CrystEngComm

Accepted Manuscript

ROYAL SOCIETY OF CHEMISTRY

www.rsc.org/crystengcomm

Cite this: DOI: 10.1039/c0xx00000x

www.rsc.org/xxxxxx

ARTICLE TYPE

High entropy alloy mediated growth of graphene

Yih-Farn Kao[+,a], Chia-I Hung[+,a], Shih-Hsin Chang[b], Jien-Wei Yeh[a], and Wen-Kuang Hsu*[a]

Received (in XXX, XXX) Xth XXXXXXXXX 20XX, Accepted Xth XXXXXXXXX 20XX
DOI: 10.1039/b000000x

Pyrolysis of acetylene over thin films made of $Cu_xFeCoNiMn$ yields graphene and sheet dimension is found to control by x. Monolayer structure forms at x = 0.5 and sheet size reaches a value as large as 600 μm^2. Layer number increases as x rises and turbostratic graphite forms at x = 1.5. The x controlled growth of graphene is supported by raman mapping, AFM and TEM.

1. Introduction

Graphene is an one-atom thick structure and shows electronic stability and mechanical strength. Experiments performed at low temperature reveal that transport through graphene does not suffer from the peierls distortion and carriers remain mobile at Dirac-point.[1] Upon loading, sp^2 bonded networks display an excellent elasticity[2] and breaking strength, estimated from load-displacement profiles, reaches a value as high as 42 N m^{-2}.[3] Graphene strength, however, is controlled by defect density and oxygenated lattice-induced cracking has been detected at low stress application.[3] Production of large graphene with low defect density has now become a important issue and various synthetic methods have been developed, including graphite exfoliation, heating of carbide, hydrocarbon pyrolysis over metal substrates, oxidative opening of carbon nanotubes and reduction of graphite oxides.[4] Among these techniques, the metal mediated growth is a low cost process and has been proved capable of controlling layer number (LN) and defect density.[4] For example, hydrocarbon pyrolysis over Cu or Ni substrates yields graphene with LN < 4 and sheet dimension is influenced by the metal grain size. Liu *et al* have recently discovered that graphene can be made by vacuum annealing of Ni_3C/Cu alloys at 900 °C and single layer formation prevails at Ni/Cu = 0.006.[4] Bi-layer graphene emerges as Ni/Cu increases to 0.01 and covers 89% of whole substrate. Carbon content in alloy plays a crucial role in controlling LN and graphene forms as a result of (i) low carbon solubility in Cu-dominated alloys and (ii) rapid diffusion of carbon to metal surfaces.

Solid solution properties of binary and tertiary alloys are known to be determined by configurational entropy which is in turn controlled by activity coefficient ($\gamma = a_c/x$) where a_c and x denote activity and mole fraction of component. At $\gamma < 1$, components are well mixed and compounds form. Mixing becomes difficult as γ exceeds 1 and clustering occurs. In both situations, the mixing induced volume change is barely distinguishable. Alloys made by equimolar mixtures of more than five elements have drawn much attention in recent years and several unique properties have been identified, including excellent hardness and high resistance to wear and corrosion.[5] Atoms with differing radii, however, cannot be orderly packed in the lattice, so atomic form factor of such a multi-element system is essentially low and the configurational entropy has been estimated to be one order of magnitude greater than that of binary and tertiary systems.[6] Materials are now termed as high-entropy alloys (HEAs) and have recently emerged at steel industry.[7] In this work, acetylene is pyrolyzed over thin films made of $Cu_xFeCoNiMn$ and large graphene with LN = 1-2 and low defect density form at x = 0.5. Defective graphite emerges as x increases and LN > 20 is detected at x = 1.5. Experiments further reveal that lattice parameter (L) varies with x and controls carbon diffusion and precipitation. The x controlled growth of graphene is supported by experimental data, including raman mapping, atomic force microscopy (AFM) and transmission electron microscopy (TEM).

2. Experimental details

HEA, consisting of Cu, Fe, Co, Ni and Mn, is used as substrates for graphene production and Cu, due to its weaker affinity to carbon, is selected as x variable. $Cu_xFeCoNiMn$ ingots hereafter defined as S_x are made by a standard arc-melting technique and are sliced into films (15 × 15 × 0.02 mm). After polishing treatment, S_x is characterized by X-ray diffraction (XRD) and scanning electron microscope (SEM). Graphene are subsequently grown through pyrolysis of acetylene and procedures are briefed as follows. First, S_x is placed in a ceramic tube and is repeatedly purged with H_2 at 200 °C. Second, the H_2/C_2H_2 (100:3 sccm) mixture is introduced into furnace and is decomposed at 900 °C for 4 min. Optical microscope reveals that a thin layer of dark material, defined as G_x, forms at S_x surfaces and repeated experiments yield a similar G_x/S_x structure. The G_x/S_x interface is then exposed by focused ion beam etching technique and is subsequently analyzed by high-resolution TEM (HRTEM), scanning tunneling microscope (STM) and X-ray photoelectron spectrometer (XPS). G_x is mechanically transferred to SiO_2 substrates according to reported method[4] and LN is measured with micro-raman spectrometer and AFM. The field emission performance of G_x is also evaluated and experiments are carried

out in a high vacuum chamber (~10^{-7} torr) equipped with electrical fit-through to measure emitting current density (J).

3. Results and discussion

3.1 *XRD of S_x substrates*

Figure 1a displays XRD profiles of S_x and reflections arising from (111), (200), (220) and (311) crystallographic planes indicate HEA to be f.c.c. structure. Enhanced (200) profiles further reveals that L is proportional to x and calculation based on Scherrer equation gives L = 3.604 Å at x = 0.5, 3.606 Å at x = 1.0 and 3.612 Å at x = 1.5, corresponding to 0.5% lattice dilation (insert). The $L \propto$ x relation also occurs in other HEAs and lattice dilates by ca. 0.01 ± 0.005 Å.[6,7] Figures 1b-d show electron backscattered SEM images of polished S_x at 5 keV beam energy and resolution is set at 60s per scan. At x = 0.5, fringe contrast is absent and grain boundaries are barely seen (Figure 1b). Microstructures, including dentrites (d) and interdentrites (id), then emerge as x increases and indicate elemental separations (Figures 1c-d). The d and id formations are owing to large negative enthalpy induced elemental clustering and are also present in various HEAs at x > 0.5, including $Al_xCoCrFeNi$, $Al_xCrFe1.5MnNi_{0.5}$, $CoFeMnTi_xVZr$ and $AlCoCrFeNiTi_x$.[8,9]

3.2 *Raman spectra and mapping of G_x*

Structures built by sp^2 carbon show an E_{2g} symmetry and the C-C stretching induced polarization, also known as G-mode, appears at 1580 cm^{-1}. A_{1g} symmetry emerges as carbon bonds are networked and defect-induced ring breathing produces phonons at zone boundary. This is called D-mode and represents the first-order scattering in graphite (1350 cm^{-1}) and the second-order scattering in graphene (2D = 2700 cm^{-1}). Study indicates that mode intensity is related to matrix-element-weighted vibrational density of states and can therefore be used as indication of crystallite size. For example, the LN is inversely proportional to 2D/G and approximates 1 at 2D/G ≈ 4.[10,11] Along in-plane direction, the crystallinity shows an inverse relationship with D/G and graphite consisting of large crystallites gives a low D/G.[12-14] Figures 2a-d show micro-raman mapping of G_x on SiO_2 substrate (50 × 50 μm) and the letters (A-H) denote regions where spectra are produced (Figure 2e). For $G_{0.5}$, the 2D-band dominated coverage is large and takes up 40% of silica substrate, corresponding to 600 μm^2 (blue, region-A, Figure 2a). Region-B, in contrast, is governed by G-band and 2D/G significantly decreases (red, Figures 2a and 2e). At x = 1, the 2D-band governed area shrinks and 2D/G in regions-C and -D decreases to 2.1 and 0.6 (Figures 2b and 2e). Turbostratic graphite then emerges as x increases to 1.5 and defective edges induced phonon scattering is evident by D-band appearance (E, F, Figures 2c and 2e). Figure 2d shows D/G mapping of $G_{1.5}$ at different x and spectral energy is counted according to Figure 2e. Clearly, D/G in regions-G and -H exceeds 1 and again verifies $G_{1.5}$ to be defective; the LN being estimated to be 20 ± 2.[11,15] Figure 2f plots 2D/G (red) and D/G (dark) at regions-A ($G_{0.5}$), -C ($G_{1.0}$), -E ($G_{1.5}$) and -G ($G_{1.5}$) and each data point represents average of five measurements. At region-A, 2D/G approximates 3.8 and decreases to 2.2 at region-C; the former corresponds to a monolayer structure. D/G, in contrast, is low and slightly increases at x = 1. The 2D/G $\propto (D/G)^{-1}$ again appears at x = 1.5 and indicates that monolayer graphene mainly forms at $S_{0.5}$ and graphite formation prevails at x > 1.0. The growth transition from monolayer graphene to turbostratic graphite at x = 1 is further supported by 2D-band broadening and full-width at half maximum (FWHM) is measured to be 31 cm^{-1} at region-A, 32 cm^{-1} at region-C, 51 cm^{-1} at region-E and 52 cm^{-1} at region-G (blue, Figure 2f).

3.3 *AFM and TEM characterizations of G_x*

Figure 3 shows AFM images of $G_{0.5}$ (a), $G_{1.0}$ (c) and $G_{1.5}$ (e) and corresponding surface roughness (b, d and f). Previous study reveals that tip-graphene interaction produces spatial offset by 0.33 ± 0.05 nm and actual thickness of a single-layer graphene lies on 0.7-1.1 nm.[16-20] AFM measurements carried out on $G_{0.5}$ give 1.06 nm; a value which approximates a single layer graphene (line A-B, Figures 3a-b) and is consistent with raman data (Figure 2a). Crystallites become thicker as x increases and multi-layer structure is supported by enhanced image contrast (bright domains, Figures 3c and 3e)[19,20]; LN being evaluated to be 4 for $G_{1.0}$ and 6 for $G_{1.5}$ according to roughness profiles. Note in $G_{1.5}$ that crystallites shrink and are interconnected, again indicative of turbostratic structure. Figure 4 shows the bright-field TEM images (a, c and e) and in-situ electron diffraction (ED) patterns (b, d and f) at G_x/S_x interfaces. At x = 0.5, ED shows alloy phase only and point groups correspond to (323) zone axis of f.c.c. structure (Figure 4b). Enhanced image further reveals that long segments of mono- and bi-layer graphene aggregate at HEA surfaces and a single layer thickness is measured to be 3.58-3.60 Å (arrows, insert, Figure 4a), consistent with reported data.[21-28] For $G_{1.0}$, the LN increases to 6-7 (insert, Figure 4c) and diffusion ring due to layer stacking fault is present (arrows, Figure 4d). Aureole then vanishes as graphene diffraction is intentionally blocked by beam aperture, again verifying thicker graphene in $G_{1.0}$ (Figure S1). Graphite structure becomes obvious in $G_{1.5}$ and shows inter-layer diffractions (Figure 4e & arrows, Figure 4f). It is worth mentioning that inter-layer spacing, due to enhanced van der Waal's force, may decrease in graphite and previous study gives 3.35 Å.[29] LN in $G_{1.5}$ exceeds 20 and layer-to-layer separation truly narrows to 3.35-3.47 Å.

3.4 *STM imaging of G_x*

Figure 5a displays HR-STM image of $G_{0.5}/S_{0.5}$ and the graphene growth on HEA surfaces is verified by honeycomb structure. The C-C bond length approximates theory (1.485 Å, circle)[29] and defects are barely seen, consistent with raman data. Again, G_x/S_x structure is evident by moiré fringes known as a result of constructive interference[30] and electronically correlated interface verifies $G_{0.5}$ to be monolayer dominated. Figure 5b shows HR-STM image recorded from the $S_{0.5}$ (110) plane which is consistent with the fast Fourier transformation (Figure 5c). First, stripe fringes support electronic correlation at graphene/HEA interface (bright regions). Second, hexagonal rings match with the periodicity of $S_{0.5}$ lattice and the ring center lies on the top of atom (insert, Figure 5c). Interfacial coupling however only occurs as the (110) plane is rotated by 23° (grey) and spacing between adjacent moiré fringes is 1.2 nm, equivalent to 6 hexagons connected along zigzag edges (yellow, Figure 5d). Figure 6

displays optical images (Olympus BX50, Fluorescence) obtained from $G_{0.5;}$ sample is deposited onto SiO_2/Si substrate (arrow 1) and graphene and graphite based on raman mapping are denoted as arrows 2 and 3. (insert, Figure 6). It is worth mentioning that acid cannot simultaneously etch five different elements (HEAs) and samples are therefore decorated with remaining grains (arrow 4).

3.5 *Bonding characterization by XPS*

Previous XPS study on Ni-produced graphene reveals that carbon dissolution into substrate causes lattice dilation and cell stresses induce Ni-2p peak shift to high energy regime.[31] HEAs, as shown in XRD profiles, display a $x \propto L$ relation and significant amount of carbidic species are therefore anticipated at x = 1.5. Figures 7a-f show XPS spectra of Cu-2p, Fe-2p, Co-2p, Ni-2p, Mn-2p and C-1s and, the peak intensity has been calibrated at ± 2%. Except Mn-2p, peaks truly shift with x and measurements give 954→955.8 eV ($2p_{1/2}$) at $Cu_{0.5}$ and 934.8→936.1 eV ($2p_{3/2}$) at $Cu_{1.5}$, corresponding to 1.8 and 1.3 eV increase in binding energy (Figure 7a). For Fe, Co, Ni and C, the binding energy at x = 0.5 and 1.5 increases by 1.1 eV ($2p_{1/2}$) and 1.2 eV ($2p_{3/2}$) (Figure 7b), by 0.2 eV ($2p_{1/2}$) and 1 eV ($2p_{3/2}$) (Figure 7c), by 0.5 eV ($2p_{1/2}$) and 0.7 eV ($2p_{3/2}$) (Figure 7d) and by 1.5 eV (Figure 7f); the C-1s peak shift again verifies carbon dissolution into S_x (insert, Figure 7f). Additional evidence in support of carbidic structures comes from XRD measurements. At x = 0.5, L is measured to be 3.462 Å and increases to 3.478 Å at x = 1.0, corresponding to 0.5% cell dilation. L then reaches 3.582 Å at x = 1.5; value which is equivalent to 9% increase in cell volume and confirms significant carbon content in S_x. Oxidation also causes cell dilation and is evident by oxide profiles at 944.8 eV for CuO-$2p_{3/2}$, 715.7 eV for Fe_2O_3-$2p_{3/2}$, 780.4 eV for CoO-$2p_{3/2}$, 873.8 eV for NiO-$2p_{1/2}$, 864.1 eV for NiO-$2p_{3/2}$ and 855.8 eV for Ni_2O_3-$2p_{3/2}$ (squares, Figures 7a-d).[32-35] It is now understood that oxygen source mainly comes from ceramic tubes and diffuses into substrate to form oxides. In this respect, graphene epoxides may be produced through thermal reduction of oxides. First, singlet oxygen captures diffusing carbon to form carbonyl groups.[36] Second, the absence of oxide phase in Mn spectrum supports thermal reduction and accounts for unchanged XPS peak position (Figure 7e). Third, MnO reduction begins at 300°C and completes at 600 °C; the latter is lower than pyrolytic temperature here.[37]

3.6 *Field emission by G_x*

A single layer graphene also means field emission from individual atoms and screening effect due to adjacent layers is absent. Figure 8 plots J as a function of applied electric field (E) (a) and corresponding Fowler-Nordheim (F-N) plot (b); the latter is based on $\ln(J/E^2) = \ln(a\beta^2/\varphi) - b\varphi^{3/2}/\beta E$ where β is the field enhancement factor, φ is the work function of the emitter (~5 eV), a is 1.54×10^{-6} A V^{-2} eV and b is 6.83×10^3 $eV^{-3/2}$ V μm^{-1}.[38] We find that turn-on-voltage follows the sequence $G_{0.5} < G_{1.0} < G_{1.5}$ and linear F-N plot confirms an E driven emission; the β being estimated to be 373 for $G_{0.5}$, 187 for $G_{1.0}$ and 130 for $G_{1.5}$ (insert, Figure 8b). These values are much lower compared with reported data on defective graphene and reflect the fact that samples here possess a low defect density.[39-42] The $\beta \propto x^{-1}$ also indicates a reduced sharpness as LN increases and emission is truly screened by adjacent layers, accounting for high turn-on-voltage and low J at $G_{1.5}$ (insert, Figure 8a & Figure 8c).

3.7 *Growth mechanism of graphene on S_x*

It has now gained general acceptance that metal mediated growth of graphene involves carbon diffusion and precipitation; the former occurs at elevated temperature and diffusion rate is controlled by (i) metal-carbon affinity and (ii) L.[11-15] Cu has a low affinity with carbon and, based on analyses above, behaves as L controlling element in S_x. Accordingly, the x must play a crucial role in determining diffusion and precipitation and the graphene growth can be described by Figure 9. At step 1, hydrocarbon precursors are thermally decomposed and carbon adsorption subsequently takes place at S_x surfaces (step 2). Carbon species then dissolves into substrates and form intermediate carbides (step 3). Note that step 1-3 is similar to catalytic production of carbon nanotubes and does not determine defect density and LN of graphene.[43] Upon cooling, lattice contracts and carbides dissociate, resulting in carbon diffusion to HEA surfaces (step 4). Takeuchi *et al* have studied atomic pairing enthalpy of different carbides and their calculations give -33 kJ/mol for Cu-C, -50 kJ/mol for Fe-C, -42 kJ/mol for Co-C, -39 kJ/mol for Ni-C and -66 kJ/mol for Mn-C, indicative of carbon releasing mainly from Cu-C, Co-C and Ni-C.[44] At x = 0.5, diffusion occurs in a small L and carbon-cation attraction is strong, thus limiting carbon precipitation at HEA surfaces. L increases as x exceeds 1 and dilated lattice facilitates diffusion and precipitation processes. At step 5, precipitated carbons begin to network and form mono- and multi-layers at x = 0.5 and > 1.0 respectively. It is worth mentioning that Ni/Cu, Au/Ni and Mo/Ni alloys also make large graphene (>600 μm^2) and carbon deposition is controlled by type of precursors and reaction duration.[1-4,45] The x controlled growth, however, has not been reported and novelty includes (i) combined processes of carbon adsorption-precipitation-diffusion and (ii) control of LN and sheet size. Meanwhile, graphene dimension determined by raman mapping is relatively accurate compared with data obtained from light microscopy. First, optical lenses often produce chromatic aberrations and the defocusing length exceeds graphene thickness. Accordingly, two sheets with boundaries overlapped may be seen as one.[4] Second, raman spectra are based on collective vibrations of C-C bonds and D/G and 2D/G directly reflect LN and grain size along a-axis. In this respect, sheet size ~ 600 μm^2 obtained here is significant (Figure 2) and proves the x controlled growth to be a promising technique.

4. Conclusions

$Cu_xFeCoNiMn$ is used as template for graphene production and sheet size is found to control by x. At x = 0.5, LN approximates 1 and defect density, as revealed by STM and J measurements, is low. Turbostratic graphite emerges as x increases and LN exceeds 20 at x = 1.5. The x-controlled growth mechanism involves five consecutive steps and each is supported by experimental data.

Acknowledgements

We thank the National Science Council of Taiwan for the financial supports (NSC-101-2112-M-007-011-MY2 and NSC-

98-2112-M-001-027-MY3). The arts were supported by Huiling Chen.

Notes and references

[a] *Department of Materials Science and Engineering, National Tsing Hua University, Hsinchu 30013, Taiwan. Fax: +886 3 5715131x35399; Tel: +886 3 5715131x35399; E-mail: wkhsu@mx.nthu.edu.tw*
[b] *Research center for Applied Science, Acadamic Sinica, Taipei 11529, Taiwan*
[+] *These authors contributed equally to this work*

† Electronic Supplementary Information (ESI) available: [details of any supplementary information available should be included here]. See DOI: 10.1039/b000000x/

‡ Footnotes should appear here. These might include comments relevant to but not central to the matter under discussion, limited experimental and spectral data, and crystallographic data.

1. X. Du, I. Skachko, A. Barker and E. Y. Andrei, *Nat Nano*, 2008, **3**, 491-495.
2. S. Park, K.-S. Lee, G. Bozoklu, W. Cai, S. T. Nguyen and R. S. Ruoff, *ACS Nano*, 2008, **2**, 572-578.
3. C. Lee, X. Wei, J. W. Kysar and J. Hone, *Science*, 2008, **321**, 385-388.
4. X. Liu, L. Fu, N. Liu, T. Gao, Y. Zhang, L. Liao and Z. Liu, *The Journal of Physical Chemistry C*, 2011, **115**, 11976-11982.
5. J. W. Yeh, S. K. Chen, S. J. Lin, J. Y. Gan, T. S. Chin, T. T. Shun, C. H. Tsau and S. Y. Chang, *Advanced Engineering Materials*, 2004, **6**, 299-303.
6. Y.-F. Kao, T.-J. Chen, S.-K. Chen and J.-W. Yeh, *Journal of Alloys and Compounds*, 2009, **488**, 57-64.
7. S.-T. Chen, W.-Y. Tang, Y.-F. Kuo, S.-Y. Chen, C.-H. Tsau, T.-T. Shun and J.-W. Yeh, *Materials Science and Engineering: A*, 2010, **527**, 5818-5825.
8. Y.-F. Kao, S.-K. Chen, J.-H. Sheu, J.-T. Lin, W.-E. Lin, J.-W. Yeh, S.-J. Lin, T.-H. Liou and C.-W. Wang, *International Journal of Hydrogen Energy*, 2010, **35**, 9046-9059.
9. Y. J. Zhou, Y. Zhang, Y. L. Wang and G. L. Chen, *Applied Physics Letters*, 2007, **90**, 181904.
10. R. J. Nemanich and S. A. Solin, *Physical Review B*, 1979, **20**, 392-401.
11. F. Tuinstra and J. L. Koenig, *The Journal of Chemical Physics*, 1970, **53**, 1126-1130.
12. A. C. Ferrari and J. Robertson, *Physical Review B*, 2000, **61**, 14095-14107.
13. A. C. Ferrari and J. Robertson, *Physical Review B*, 2001, **64**, 075414.
14. C. Thomsen and S. Reich, *Physical Review Letters*, 2000, **85**, 5214-5217.
15. M. M. Lucchese, F. Stavale, E. H. M. Ferreira, C. Vilani, M. V. O. Moutinho, R. B. Capaz, C. A. Achete and A. Jorio, *Carbon*, 2010, **48**, 1592-1597.
16. A. Ismach, C. Druzgalski, S. Penwell, A. Schwartzberg, M. Zheng, A. Javey, J. Bokor and Y. Zhang, *Nano Letters*, 2010, **10**, 1542-1548.
17. X. Li, X. Wang, L. Zhang, S. Lee and H. Dai, *Science*, 2008, **319**, 1229-1232.
18. H. Park, P. R. Brown, V. Bulović and J. Kong, *Nano Letters*, 2011, **12**, 133-140.
19. A. Reina, X. Jia, J. Ho, D. Nezich, H. Son, V. Bulovic, M. S. Dresselhaus and J. Kong, *Nano Letters*, 2008, **9**, 30-35.
20. A. Gupta, G. Chen, P. Joshi, S. Tadigadapa and Eklund, *Nano Letters*, 2006, **6**, 2667-2673.
21. T. Kato and R. Hatakeyama, *Nat Nano*, 2012, **7**, 651-656.
22. G. Radhakrishnan, J. D. Cardema, P. M. Adams, H. I. Kim and B. Foran, *Journal of The Electrochemical Society*, 2012, **159**, A752-A761.
23. C.-Y. Su, A.-Y. Lu, C.-Y. Wu, Y.-T. Li, K.-K. Liu, W. Zhang, S.-Y. Lin, Z.-Y. Juang, Y.-L. Zhong, F.-R. Chen and L.-J. Li, *Nano Letters*, 2011, **11**, 3612-3616.
24. C. Vecchio, S. Sonde, C. Bongiorno, M. Rambach, R. Yakimova, V. Raineri and F. Giannazzo, *Nanoscale Research Letters*, 2011, **6**, 269.
25. D. Wang, R. Kou, D. Choi, Z. Yang, Z. Nie, J. Li, L. V. Saraf, D. Hu, J. Zhang, G. L. Graff, J. Liu, M. A. Pope and I. A. Aksay, *ACS Nano*, 2010, **4**, 1587-1595.
26. W. Lu, R. Barbosa, E. Clarke, K. Eyink, L. Grazulis, W. C. Mitchel and J. J. Boeckl, *The Journal of Physical Chemistry C*, 2012, **116**, 15342-15347.
27. W. Norimatsu and M. Kusunoki, *Chemical Physics Letters*, 2009, **468**, 52-56.
28. H. Yoon, T. Kang, J. M. Lee, S.-i. Kim, K. Seo, J. Kim, W. I. Park and B. Kim, *The Journal of Physical Chemistry Letters*, 2011, **2**, 956-960.
29. X. Weng, J. A. Robinson, K. Trumbull, R. Cavalero, M. A. Fanton and D. Snyder, *Applied Physics Letters*, 2010, **97**, 201905-201903.
30. S. Marchini, S. Günther and J. Wintterlin, *Physical Review B*, 2007, **76**, 075429.
31. R. S. Weatherup, B. C. Bayer, R. Blume, C. Ducati, C. Baehtz, R. Schlögl and S. Hofmann, *Nano Letters*, 2011, **11**, 4154-4160.
32. R. K. Tandon, R. Payling, B. E. Chenhall, P. T. Crisp, J. Ellis and R. S. Baker, *Applications of Surface Science*, 1985, **20**, 527-537.
33. J. Haber and L. Ungier, *Journal of Electron Spectroscopy and Related Phenomena*, 1977, **12**, 305-312.
34. A. N. Mansour, *Surface Science Spectra*, 1994, **3**, 231-238.
35. K. S. Kim and N. Winograd, *Surface Science*, 1974, **43**, 625-643.
36. J.-L. Li, K. N. Kudin, M. J. McAllister, R. K. Prud'homme, I. A. Aksay and R. Car, *Physical Review Letters*, 2006, **96**, 176101.
37. Y. Zhao, G. Zhu and Z. Cheng, *Hydrometallurgy*, 2010, **105**, 96-102.
38. D. D. B. Williams and C. B. Carter, *Transmission Electron Microscopy 4 Vol Set: A Textbook for Materials Science*, Plenum Press, 1996.
39. J. Dong, B. Zeng, Y. Lan, S. Tian, Y. Shan, X. Liu, Z. Yang, H. Wang and Z. F. Ren, *Journal of Nanoscience and Nanotechnology*, 2010, **10**, 5051-5055.
40. Z.-S. Wu, S. Pei, W. Ren, D. Tang, L. Gao, B. Liu, F. Li, C. Liu and H.-M. Cheng, *Advanced Materials*, 2009, **21**, 1756-1760.
41. C. Wu, F. Li, Y. Zhang and T. Guo, *Vacuum*, 2013, **94**, 48-52.
42. C. Wu, F. Li, Y. Zhang and T. Guo, *Thin Solid Films*, 2013, **544**, 399-402.
43. M. Terrones, N. Grobert, J. Olivares, J. P. Zhang, H. Terrones, K. Kordatos, W. K. Hsu, J. P. Hare, P. D. Townsend, K. Prassides, A. K. Cheetham, H. W. Kroto and D. R. M. Walton, *Nature*, 1997, **388**, 52-55.
44. A. Takeuchi and A. Inoue, *MATERIALS TRANSACTIONS*, 2005, **46**, 2817-2829.
45. S. Bhaviripudi, X. Jia, M. S. Dresselhaus and J. Kong, *Nano Letters*, 2010, **10**, 4128-4133.

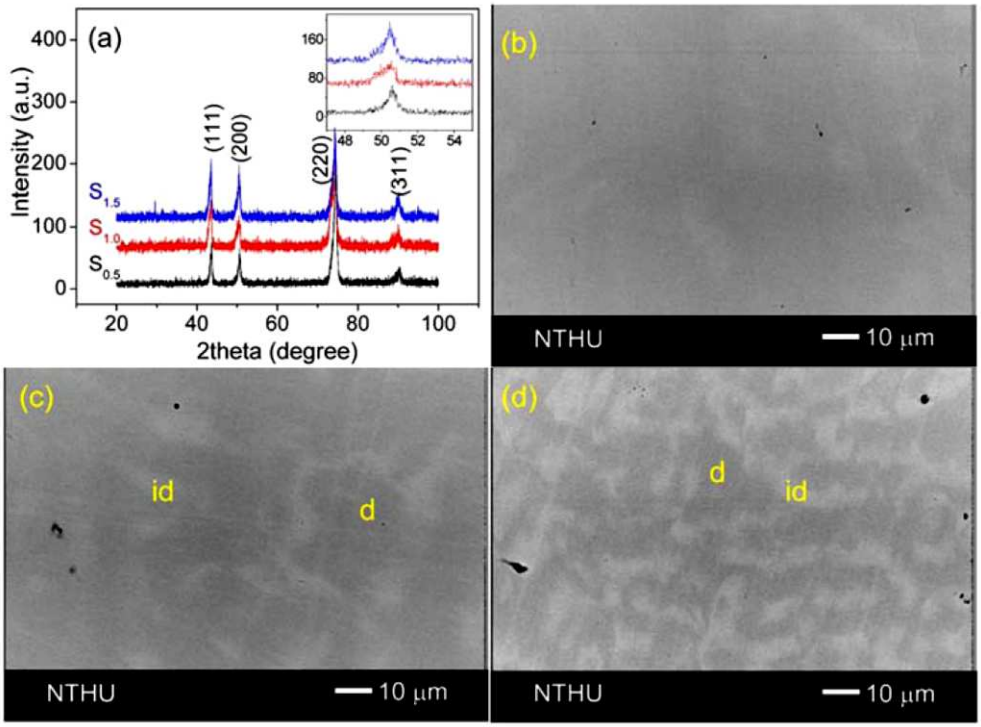

Figure 1. XRD profiles of $S_{0.5}$ (dark), $S_{1.0}$ (red) and $S_{1.5}$ (blue) (a), and corresponding electron backscattered images (b-d). Insert shows enhanced (200) reflection and the d and id denote dentrite and interdentrite structures.

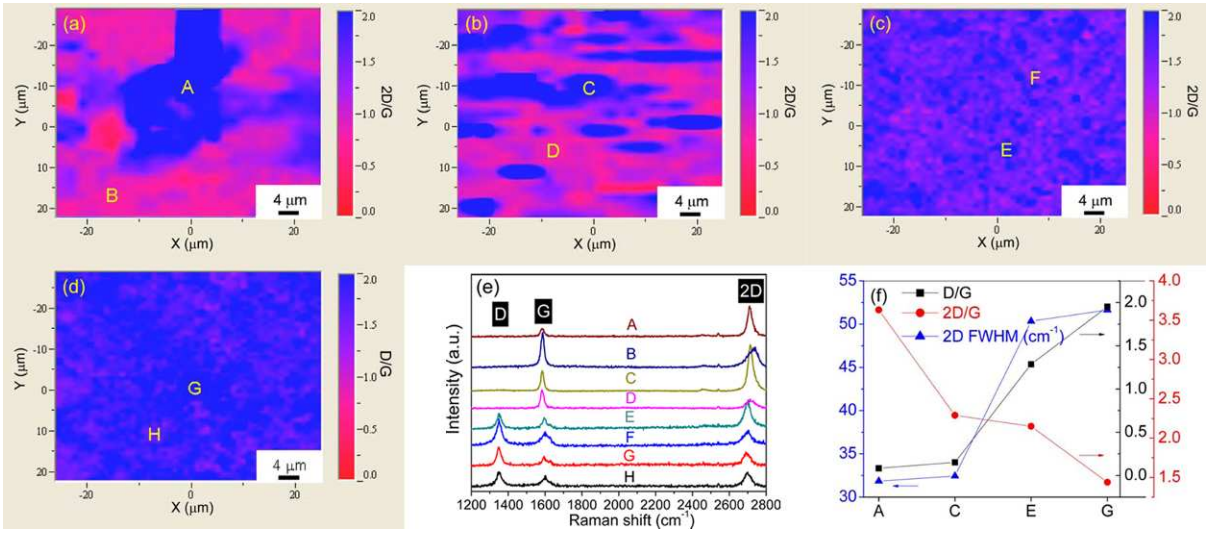

Figure 2. 2D/G mapping profiles of $G_{0.5}/S_{0.5}$ (a), $G_{1.0}/S_{1.0}$ (b) $G_{1.5}/S_{1.5}$ (c) and D/G mapping of $G_{1.5}/S_{1.5}$ (d). Raman spectra obtained from labeled regions in mapping profiles (e). Band intensity of 2D/G (red), D/G (dark) and FWHM (blue) at regions-A, -C, -E and -G (f).

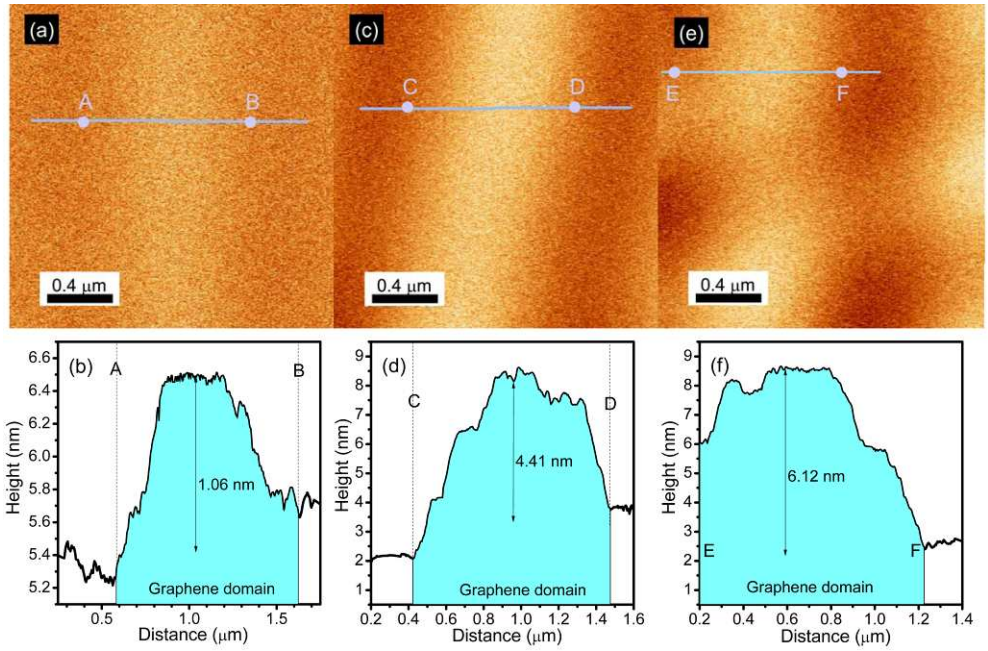

Figure 3. AFM images of $G_{0.5}$ (a), $G_{1.0}$ (c), $G_{1.5}$ (e) and corresponding surface roughness profiles (b, d and f).

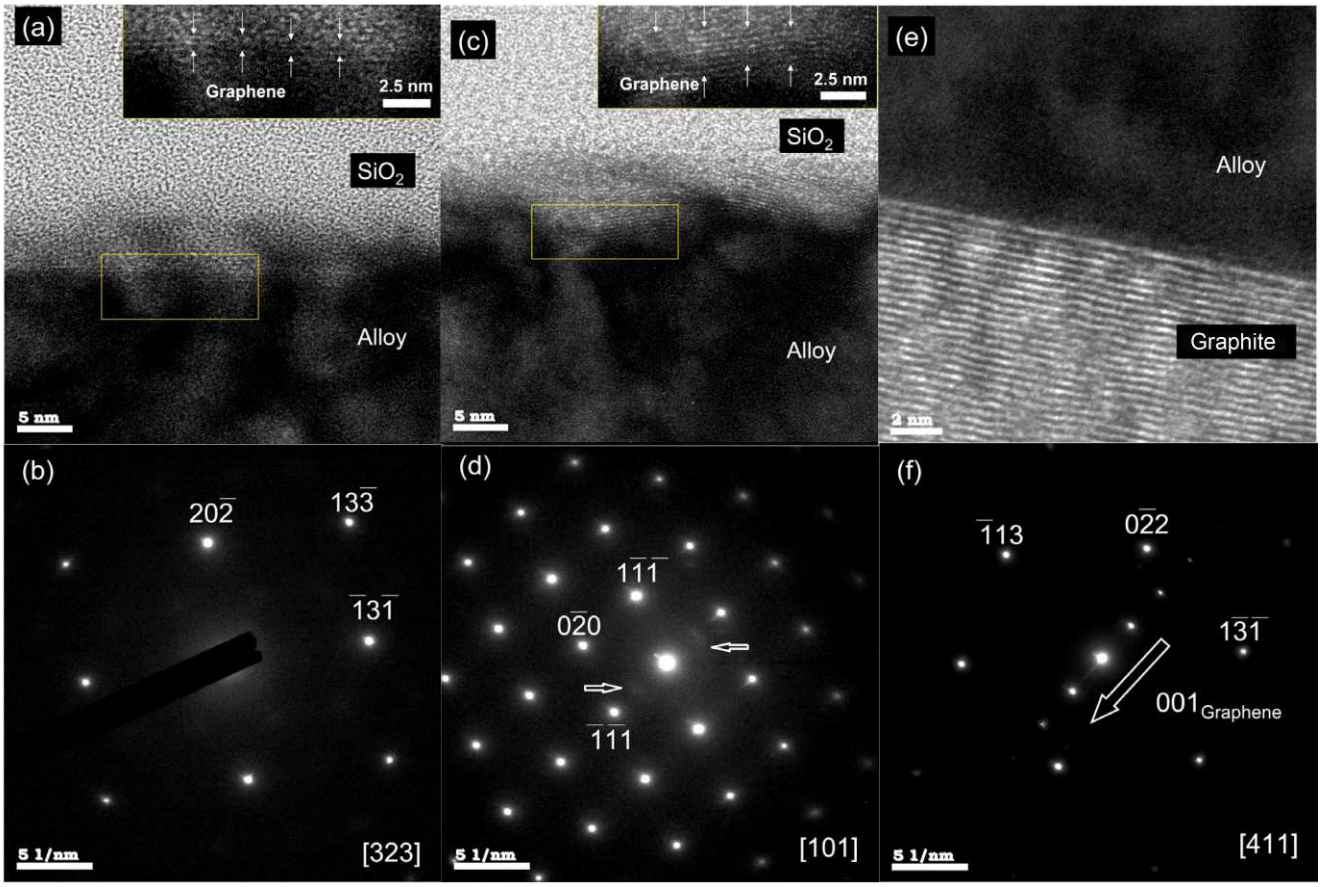

Figure 4. Bright-field TEM images of $G_{0.5}/S_{0.5}$ (a) $G_{1.0}/S_{1.0}$ (c), $G_{1.5}/S_{1.5}$ (e) and corresponding ED (b, d and f) at G_x/S_x interfaces. Inserts show enhanced images of yellow rectangles labeled in (a) and (c), respectively.

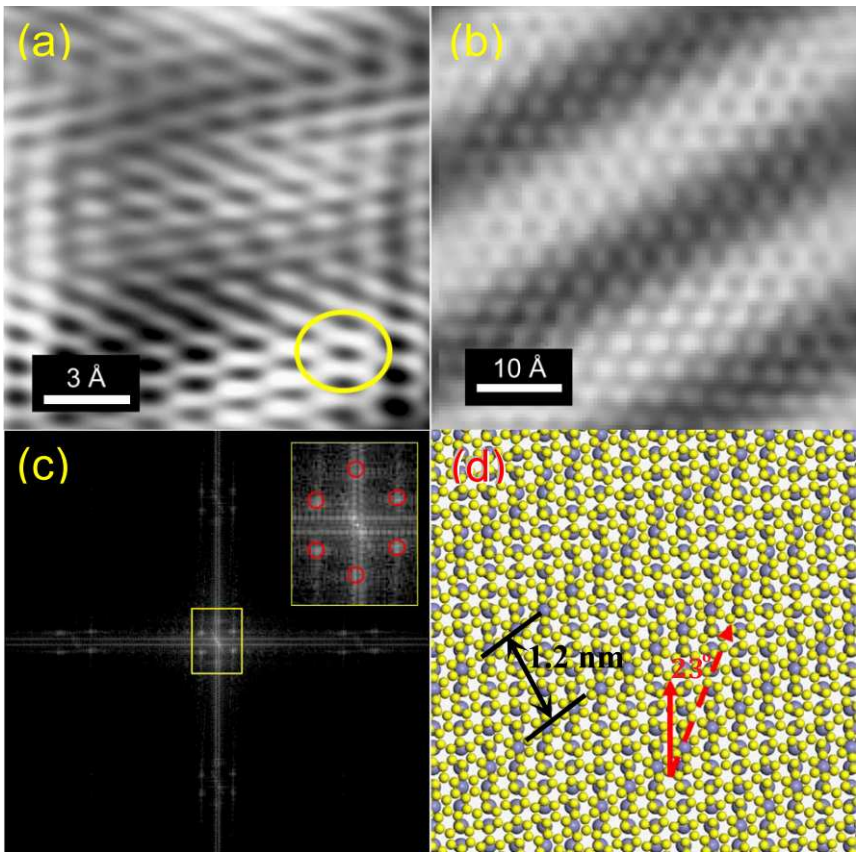

Figure 5. STM image obtained from $G_{0.5}$ (a), Moiré fringes established from $S_{0.5}$ (110) plane (b), the fast Fourier transform image (c), and the sketch of $S_{0.5}$ (110) graphene (yellow) rotated by 23° with respect to $S_{0.5}$ (110) plane (grey) (d). Arrow denotes spacing between Moiré fringes. Insert shows enlarged image of yellow rectangle marked in (c).

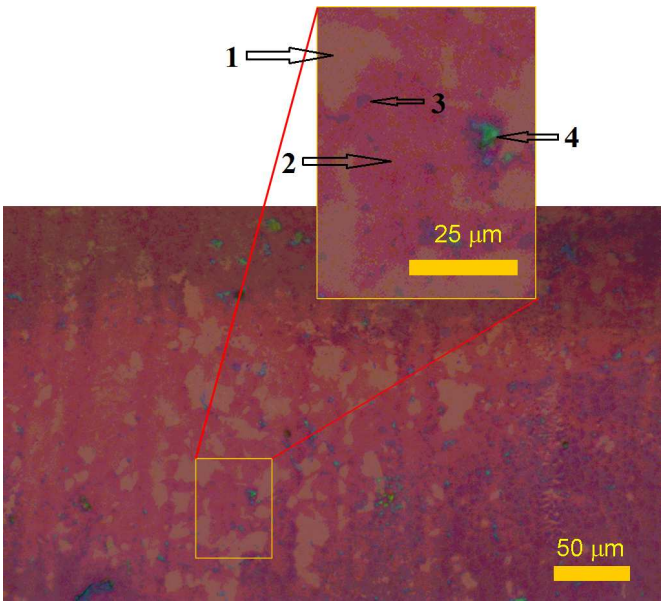

Figure 6. Optical images obtained from $G_{0.5}$ deposited onto SiO_2/Si substrate (arrow 1) and graphene and graphite based on reman mapping are denoted as arrows 2 and 3 (insert). Arrow 4 is remaining HEA particles.

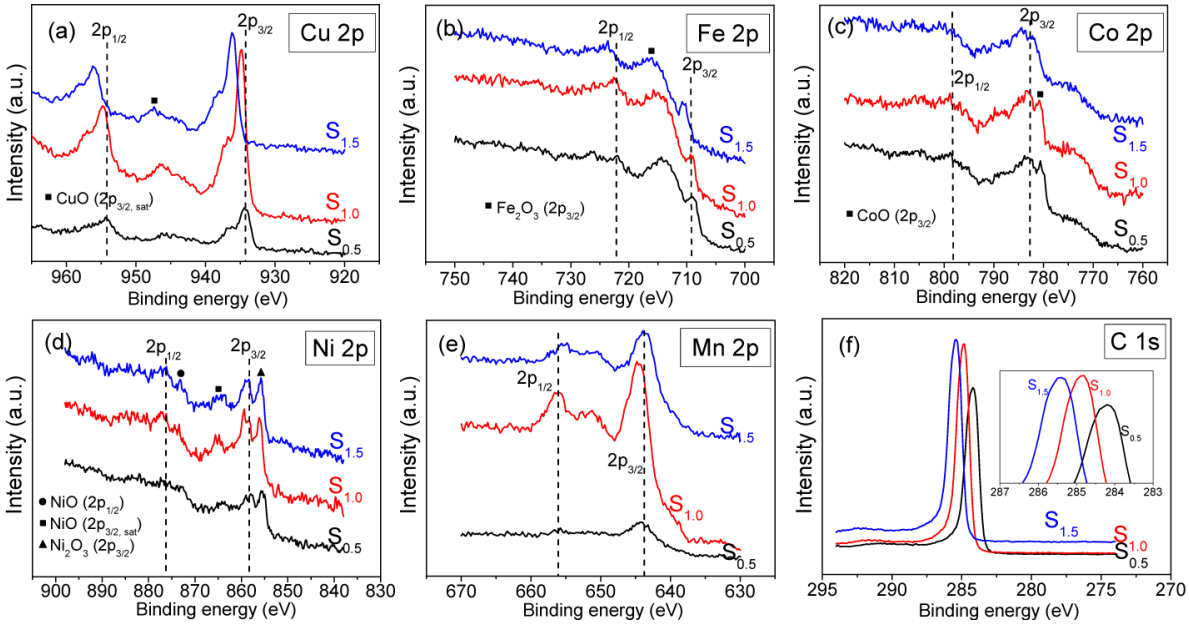

Figure 7. XPS spectra of Cu (a), Fe (b), Co (c), Ni (d), Mn (e) and C (f). Insert highlights C-1s peaks from G_x

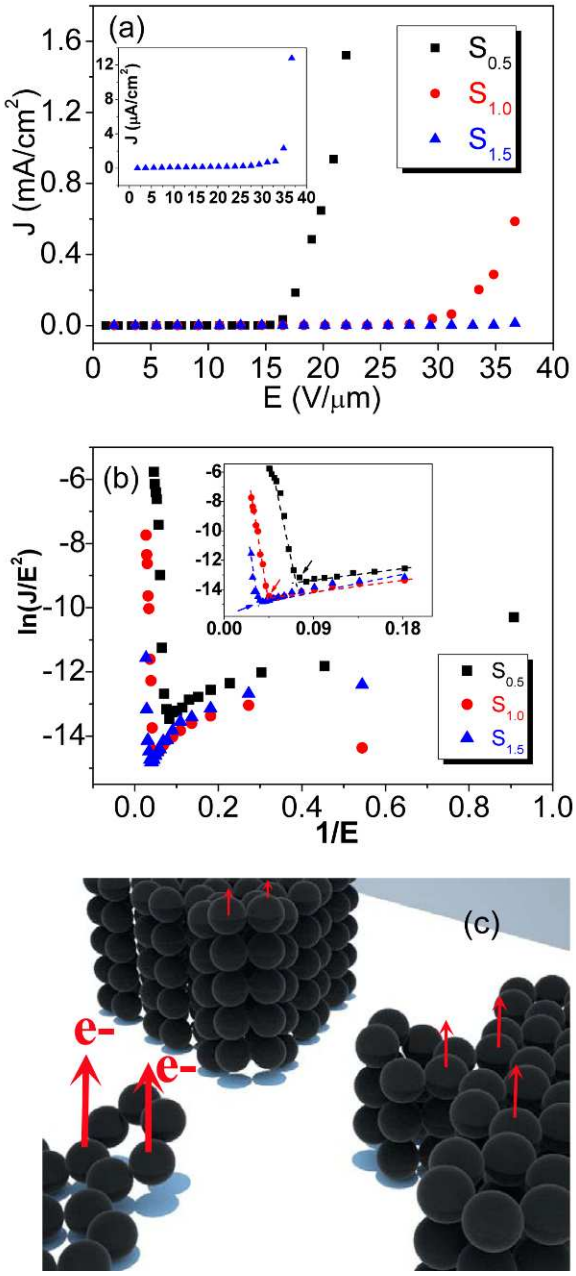

Figure 8. Field emission profiles of G_x/S_x (a), corresponding F-N plots (b) and emission structures from a single-, few- and multi-layer graphene (c). Inserts: enlarged profiles.

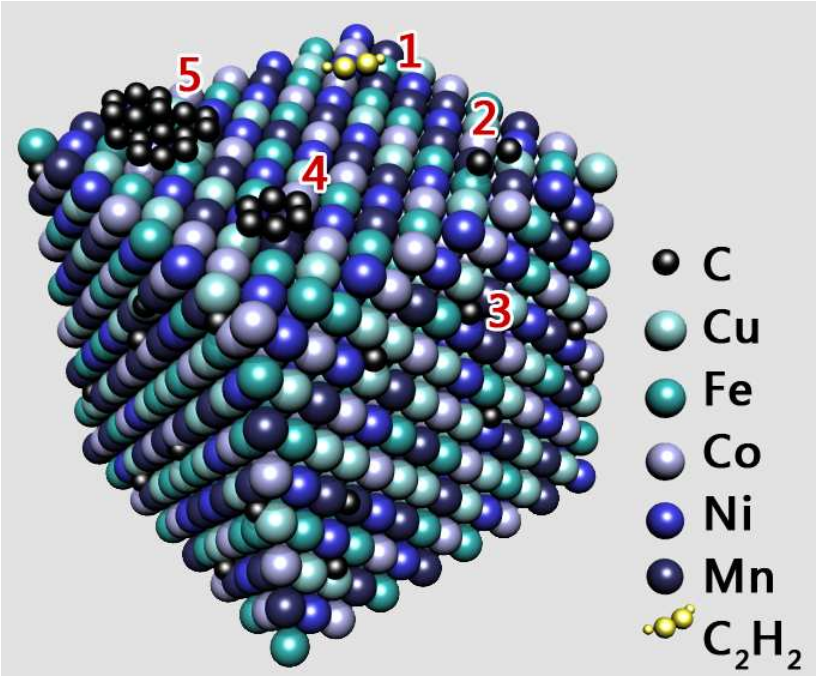

Figure 9. Growth mechanism of graphene on S_x. Step-1: thermal decomposition of hydrocarbons on S_x. Step-2: carbon adsorption onto S_x. Step-3: carbon dissolution into substrate. Step-4: cooling induced lattice contraction and carbon diffusion to S_x surfaces. Step-5: networking of surface carbon species.

Graphic entry for the Table of Contents

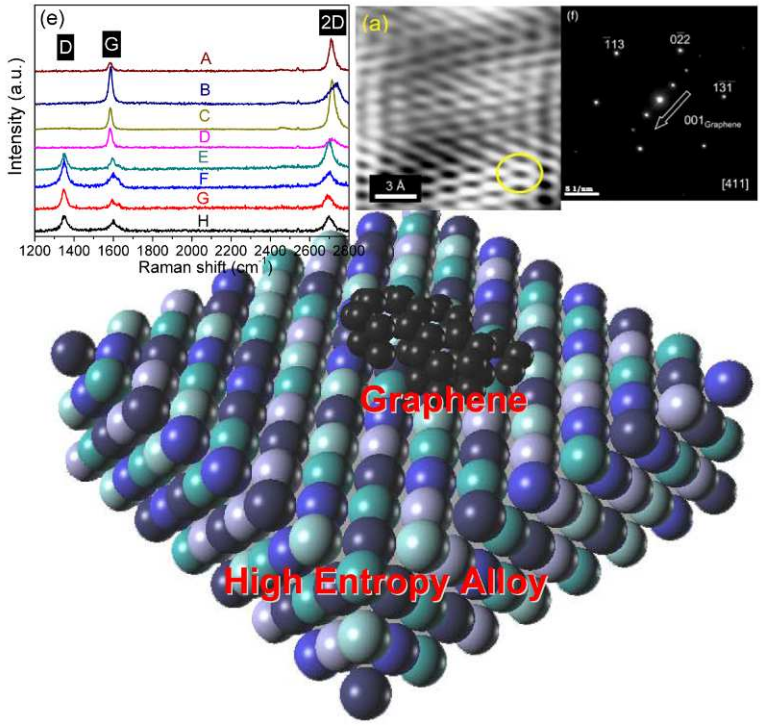

Pyrolysis of acetylene over thin films made of $Cu_xFeCoNiMn$ yields graphene and sheet dimension is found to control by x. Monolayer structure forms at x = 0.5 and sheet size reaches a value as large as 600 μm^2.